

## Structural and electrical properties of lead free ceramic: $\text{Ba}(\text{Nd}_{1/2}\text{Nb}_{1/2})\text{O}_3$

K. Amar Nath<sup>1a</sup>, K. Prasad<sup>\*1</sup>, K.P. Chandra<sup>2b</sup> and A.R. Kulkarni<sup>3c</sup>

<sup>1</sup>University Department of Physics, T.M. Bhagalpur University, Bhagalpur 812007, India

<sup>2</sup>Department of Physics, S.M. College, Bhagalpur 812001, India

<sup>3</sup>Department of Metallurgical Engineering and Materials Science, Indian Institute of Technology, Mumbai 400076, India

(Received November 17, 2012, Revised January 16, 2012, Accepted April 25, 2013)

**Abstract.** Impedance and electrical conduction studies of  $\text{Ba}(\text{Nd}_{1/2}\text{Nb}_{1/2})\text{O}_3$  ceramic prepared using conventional high temperature solid-state reaction technique are presented. The crystal symmetry, space group and unit cell dimensions were estimated using Rietveld analysis. X-ray diffraction analysis indicated the formation of a single-phase cubic structure with space group  $Pm\bar{3}m$ . Energy dispersive X-ray analysis and scanning electron microscopy studies were carried to study the quality and purity of compound. The circuit model fittings were carried out using the impedance data to find the correlation between the response of real system and idealized model electrical circuit. Complex impedance analyses suggested the dielectric relaxation to be of non-Debye type and negative temperature coefficient of resistance character. The correlated barrier hopping model was employed to successfully explain the mechanism of charge transport in  $\text{Ba}(\text{Nd}_{1/2}\text{Nb}_{1/2})\text{O}_3$ . The ac conductivity data were used to evaluate the density of states at Fermi level, minimum hopping length and apparent activation energy.

**Keywords:** ceramics; perovskite; lead-free; permittivity; impedance analysis; electrical conductivity

### 1. Introduction

In recent years, a number of lead free ternary perovskites with the general formula  $\text{A}(\text{B}'_{1/2}\text{B}''_{1/2})\text{O}_3$  have been investigated for their possible applications in electronic and/or microelectronic devices. Among these, rare-earth based niobates and/or tantalates are especially useful for microwave applications such as dielectric resonators in wireless communication systems, global positioning systems, cellular phones, etc. (Zurmiihlen *et al.* 1995a, Zurmiihlen *et al.* 1995b, Sreemoolanathan *et al.* 1997, Khalam *et al.* 2004, Dias *et al.* 2006, Khalam and Sebastian 2006). The information about the electrical properties of  $\text{Ba}(\text{Re}_{1/2}\text{Nb}_{1/2})\text{O}_3$  (Re  $\equiv$  rare-earth ions) especially in radio frequency region is still not complete and consistent. Among these

---

\*Corresponding author, Scientist, E-mail: [karn190@gmail.com](mailto:karn190@gmail.com)

<sup>a</sup>Scientist, E-mail: [karn190@gmail.com](mailto:karn190@gmail.com)

<sup>b</sup>Assistant Professor

<sup>c</sup>Professor

Ba(Nd<sub>1/2</sub>Nb<sub>1/2</sub>)O<sub>3</sub> (abbreviated hereafter as BNN) belongs to perovskite family (ABO<sub>3</sub>-type) with cubic symmetry at ambient temperature. Recently, preparation, characterization and microwave dielectric properties of BNN ceramic were carried out by Khalam *et al.* 2004. In another study, the evaluation of crystal structure and phonon modes of BNN taken up by Dias *et al.* (2006) while Kumar *et al.* (2012) studied the electrical properties of BNN having the tetragonal structure. However, the information about the electrical properties of BNN is still not complete and consistent. The study of electrical conductivity in such compounds is very important since the associated physical properties are dependent on the nature and magnitude of conductivity in these materials. Therefore, to have knowledge about the performance of BNN, it becomes important to know the carrier transport mechanism and hence the system deserved further investigation. Accordingly, the present work reports the structural (X-ray and its Rietveld analysis), microstructural (SEM and EDAX), dielectric, impedance, electric modulus and ac conductivity studies of Ba(Nd<sub>1/2</sub>Nb<sub>1/2</sub>)O<sub>3</sub>. For better understanding the correlation between the response of the real system and idealized model circuit composed of discrete electrical components, circuit model fittings, using the impedance data, have been carried. The correlated barrier hopping model has been applied to the ac conductivity data to ascertain the conduction mechanism of charge transport in the system. Also, the ac conductivity data have been used to estimate the apparent activation energy, density of states at Fermi level and minimum hopping length.

## 2. Coupled finite element / reproducing kernel approximation

Polycrystalline Ba(Nd<sub>1/2</sub>Nb<sub>1/2</sub>)O<sub>3</sub> having the tolerance factor ( $t = [(r_{Ba} + r_O)/\sqrt{2}][(r_{Nd} + r_{Nb})/2 + r_O]^{-1} = 0.9671$ ; here  $r_{Ba}$ ,  $r_{Nd}$ ,  $r_{Nb}$  and  $r_O$  are the ionic radii of the constituent ions) was prepared from AR grade (99.9%+pure, Merck) chemicals (BaCO<sub>3</sub>, Nd<sub>2</sub>O<sub>3</sub> and Nb<sub>2</sub>O<sub>5</sub>) using solid-state reaction technique at 1375°C for 7 h under a controlled heating and cooling cycles. The powder sample was then pressed (650 MPa) in the cylindrical die to obtain pellet having diameter 9.54 mm and height 1.67 mm. The pellet was subsequently heated up to 1400°C under air atmosphere for 5 h. The density of sintered pellet was determined using its geometrical measurements and water immersion (Archimedes) technique. The density of the ceramic obtained was found to be 90.6% of the theoretical one. The completion of reaction and the formation of desired compound were checked by X-ray diffraction (XRD) technique.

The XRD spectrum was taken on sintered pellet of BNN with an X-ray diffractometer (XPRT-PRO, Pan Analytical) at room temperature, using CuK<sub>α</sub> radiation ( $\lambda = 1.5406\text{Å}$ ), over a wide range of Bragg angles ( $25^\circ \leq 2\theta \leq 90^\circ$ ) with a scanning speed of  $5.08^\circ \text{ min}^{-1}$ . The XY (2θ versus intensity) data obtained from this experiment were plotted with the WinPLOTR program and the angular positions of the peaks were obtained with the same program. The dimensions of the unit cell,  $hkl$  values and space group of BNN was obtained using the DICVOL program in the FullProf 2000 software package and then refinement was carried out through the profile matching routine of FullProf. The Bragg peaks were modeled with pseudo-Voigt function and the background was estimated by linear interpolation between selected background points. The crystallite size ( $D$ ) and the Lattice strain of BNN were estimated by analyzing the broadening of XRD peaks, using Williamson–Hall approach:  $\eta \cos\theta = (K\lambda/D) + 2(\Delta\xi/\xi)\sin\theta$ ; where  $\eta$  is diffraction peak width at half intensity (FWHM) and  $\Delta\xi/\xi$  is the Lattice strain and  $K$  is the Scherrer constant (0.89). The term  $K\lambda/D$  represents the Scherrer particle size distribution. The microstructure and energy dispersive X-ray (EDAX) of the sintered BNN sample was taken on the fractured surface using a computer

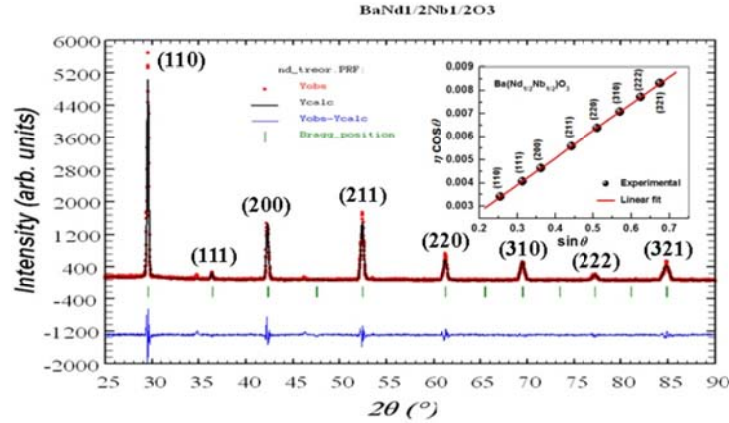


Fig. 1 Rietveld refined pattern of  $Ba(Nd_{1/2}Nb_{1/2})O_3$  in space group  $Pm\bar{3}m$ . Symbols represent observed data points and solid lines their Rietveld fit. Inset shows Williamson–Hall plot

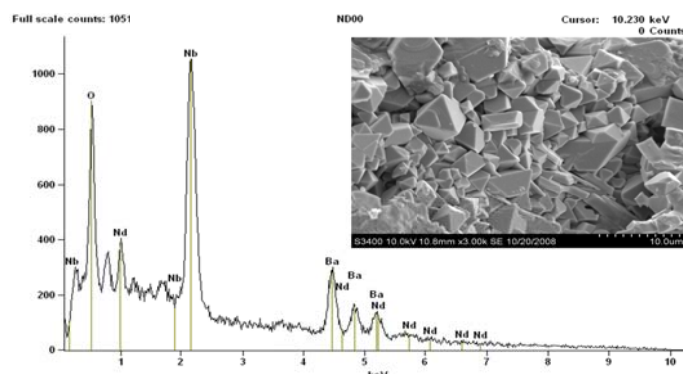
controlled scanning electron microscope (SEM Hitachi S-3400N, Japan). The SEM image analysis was carried out using UTHSCSA ImageTool 3.0 software. Real and imaginary parts of the dielectric constant and impedance were obtained as a function of frequency (1 Hz–1 MHz) and temperature (50°C–450°C) using a computer interfaced Solartron SI1260 impedance/gain phase analyzer in a cooling cycle on a symmetrical cell of type Ag|BNN|Ag, where Ag is a conductive paint coated on either side of the pellet. The temperature was varied at a rate of 1°C min<sup>-1</sup>. The real and imaginary parts ac conductivity data were obtained using the relations:  $\sigma' = \omega\epsilon_0\epsilon''$  and  $\sigma'' = \omega\epsilon_0\epsilon'$ ; where  $\epsilon'$  and  $\epsilon''$  are the real and imaginary parts of the dielectric constant respectively.

### 3. Results and discussion

#### 3.1 Structural and microstructural studies

Rietveld refinements on the X-ray (XRD) data of BNN were done by selecting the space group  $Pm\bar{3}m$ . Fig. 1 illustrates the observed, estimated and difference XRD profiles for BNN after final cycle of refinement. It can be seen that the profiles for observed and calculated one are perfectly matching. The value of  $\chi^2$  comes out to be 2.71, which is considered to be very good for estimations. The profile fitting procedure adopted was minimizing the  $\chi^2$  function. The XRD analyses indicated that BNN has a cubic unit cell structure. The crystal data and refinement factors of BNN obtained from XRD data are depicted in Table 1. The inset of Fig. 1 shows the Williamson-Hall plot for BNN. A linear least square fitting to  $\eta\cos\theta$ – $\sin\theta$  data yielded the values of average crystallite size and lattice strain respectively to be 312.75 nm and 0.0058.

To confirm the purity of chemical composition of BNN, EDAX was carried out. Fig. 2 shows the SEM image and EDAX pattern of fractured surface of sintered BNN. All the peaks in the EDAX pattern have perfectly assigned to the elements present in  $Ba(Nd_{1/2}Nb_{1/2})O_3$ . This clearly indicated the purity and formation of the phase of BNN. The grain shapes are clearly visible in the SEM image of sintered BNN sample, indicating the existence of polycrystalline microstructure. The grain of unequal sizes (about 1–5  $\mu\text{m}$ ) appears to be distributed throughout the sample.

Fig. 2 EDAX spectrum and SEM image (inset) of Ba(Nd<sub>1/2</sub>Nb<sub>1/2</sub>)O<sub>3</sub> ceramicTable 1 The crystal data and refinement factors of Ba(Nd<sub>1/2</sub>Nb<sub>1/2</sub>)O<sub>3</sub> obtained from X-ray powder diffraction data

Parameters	Results	Description of parameters
Crystal System	Cubic	$R_p$ (profile factor) = $100[\sum y_i - y_{ic}  / \sum y_i ]$ , where $y_i$ is the observed intensity and $y_{ic}$ is the calculated intensity at the $i^{\text{th}}$ step.
Space group	$Pm\bar{3}m$	$R_{wp}$ (weighted profile factor) = $100[\sum\omega_i y_i - y_{ic} ^2 / \sum\omega_i(y_i)^2]^{1/2}$ , where $\omega_i = 1/\sigma_i^2$ and $\sigma_i^2$ is variance of the observation.
$a$ (Å)	4.2716	$R_{exp}$ (expected weighted profile factor) = $100[(n-p)/\sum\omega_i(y_i)^2]^{1/2}$ , where $n$ and $p$ are the number of profile points and refined parameters, respectively.
$V$ (Å <sup>3</sup> )	77.9426	$R_B$ (Bragg factor) = $100[\sum I_{obs} - I_{calc}  / \sum I_{obs} ]$ , where $I_{obs}$ is the observed integrated intensity and $I_{calc}$ is the calculated integrated intensity.
$R_p$	29.7	$R_F$ (crystallographic $R_F$ factor) = $100[\sum F_{obs} - F_{calc}  / \sum F_{obs} ]$ , where $F$ is the structure factor, $F = \sqrt{I/L}$ , where $L$ is Lorentz polarization factor.
$R_{wp}$	25.9	$\chi^2 = \sum\omega_i(y_i - y_{ic})^2$ .
$R_{exp}$	15.7	$d$ (Durbin-Watson statistics) = $\sum\{[\omega_i(y_i - y_{ic}) - \omega_{i-1}(y_{i-1} - y_{i-1} - y_{i-1} - y_{i-1})]^2\} / \sum[\omega_i(y_i - y_{ic})]^2$ .
$R_B$	0.646E-3	$Q_D = \text{expected } d$ .
$R_F$	0.330E-3	$S$ (goodness of fit) = $(R_{wp}/R_{exp})$ .
$\chi^2$	2.71	
$d$	0.9824	
$Q_D$	1.8891	
$S$	1.6497	
$D$ (Å)	312.75	
$\Delta\xi/\xi$	0.0058	

### 3.2 Dielectric studies

Fig. 3 shows the frequency dependence of  $\epsilon'$  and  $\epsilon''$  at different temperatures. It is observed that both  $\epsilon'$  and  $\epsilon''$  follows inverse dependence on frequency. Dispersion with relatively high dielectric constant can be seen in the  $\epsilon' - f$  graph in the lower frequency region and the dielectric constant drops at high frequencies. This may be due to the space charge contribution.

At very low frequencies, dipoles follow the field and we have  $\epsilon' \approx \epsilon''$  (value of dielectric constant at quasi static fields). As the frequency increases dipoles begin to lag behind the field and  $\epsilon'$  slightly decreases. When frequency reaches the characteristic frequency, the dielectric constant drops (relaxation process) and at very high frequencies, dipoles can no longer follow the field and  $\epsilon' \approx \epsilon_\infty$ .

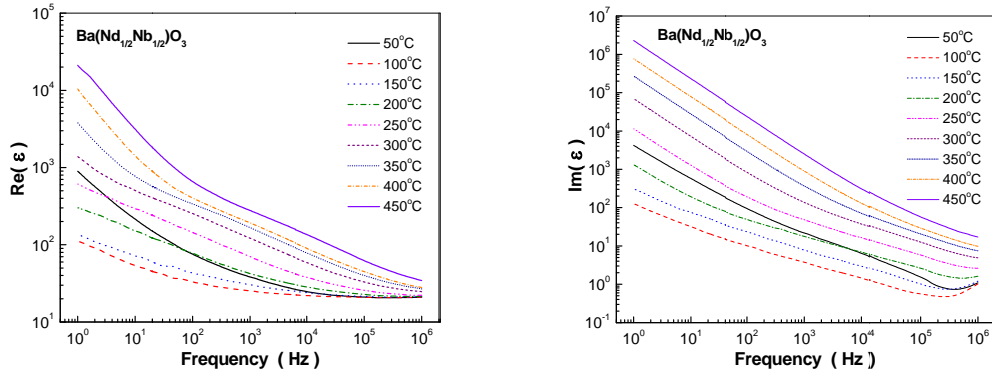


Fig. 3 Frequency dependence of real and imaginary parts of dielectric constant of  $Ba(Nd_{1/2}Nb_{1/2})O_3$  ceramic at different temperatures

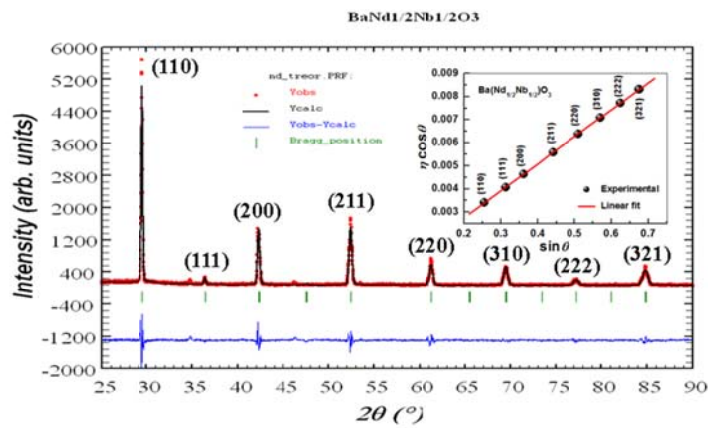


Fig. 4 Temperature dependence of real and imaginary parts of dielectric constant of  $Ba(Nd_{1/2}Nb_{1/2})O_3$  at different frequencies

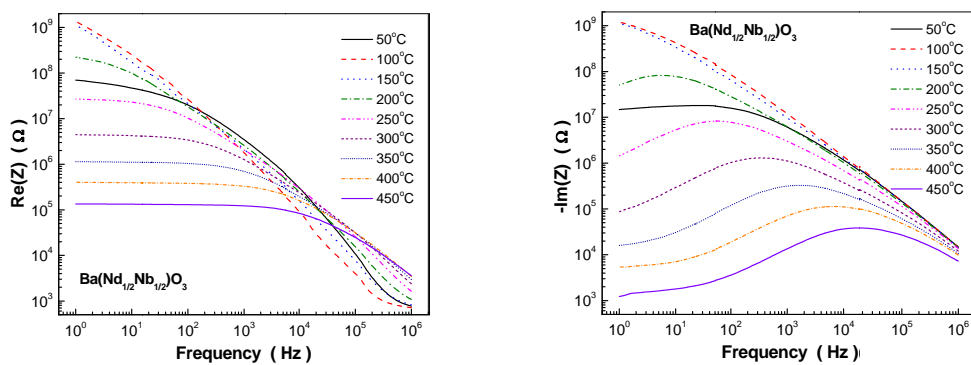


Fig. 5 Frequency dependence of real and imaginary parts of impedance of  $Ba(Nd_{1/2}Nb_{1/2})O_3$  ceramic at different temperatures

Fig. 4 illustrates the temperature dependence of  $\epsilon'$  and  $\epsilon''$  of BNN at different frequencies. The values of both  $\epsilon'$  and  $\epsilon''$  found to first decrease and then they increase with the increase in temperature. Also, BNN is found to have low  $\epsilon'$  (= 39) as well as low  $\epsilon''$  (= 21) at 1 kHz. This result is in consistent with the general observation that the dielectric constants for materials having cubic structures must be very small (Prasad *et al.* 2010a, AmarNath *et al.* 2012).

### 3.3 Flexural strength

Fig. 5 shows the variation of the real ( $Z'$ ) and imaginary ( $Z''$ ) parts of impedance with frequency at different temperatures. It is observed that the magnitude of  $Z'$  decreases with the increase in frequency indicates an increase in ac conductivity with the rise in frequency. Further, at low frequencies the  $Z'$  values flatten with rise in temperature. The values of  $Z''$  decreases with frequency at lower temperatures and at 200°C onwards the  $Z''$  values reach a maximum peak ( $Z''_{\max}$ ) which shifts to higher frequency side with increasing temperature. At a temperature 300°C onwards indication of second peak can be seen, which may be due to the grain boundary effect. A typical peak-broadening, which is slightly asymmetrical in nature, can be observed with the rise in temperature. The broadening of peaks in frequency explicit plots of  $Z''$  suggests that there is a spread of relaxation times i.e., the existence of a temperature dependent electrical relaxation phenomenon in the material is exhibited.

Fig. 6 shows the plot of scaled  $Z''$  versus reduced frequency,  $f/f_{\max}$ . It can be seen that the scaled data points coalesced into a master curve. The value of full width at half maximum (FWHM) is found to be  $>1.14$  decades. These observations indicate that the distribution function for relaxation times is nearly temperature independent with non-exponential conductivity relaxation, which suggests the possibility of ion migration that takes place via hopping accompanied by a consequential time dependent mobility of other charge carriers of the same type in the vicinity (Prasad *et al.* 2005). The most probable frequency  $\omega_m$  was obtained from the frequency at which  $Z''_{\max}$  is observed. At the peak, the relaxation is defined as:  $\omega_m\tau = 1$ , where  $\tau$  is the relaxation time which follows the Arrhenius law given by:  $\tau = \tau_0 \exp(-U/k_B T)$ , where  $\tau_0$  is the pre-exponential factor and  $U$  is the activation energy. The inset of Fig. 6 shows a plot of  $\log \tau$  versus  $1/T$ . The value of  $\tau_0$  and  $U$  are estimated using linear least squares fit to the data points shown in the inset of Fig. 6 and are, respectively, estimated to be 11.90 ns and 0.308 eV.

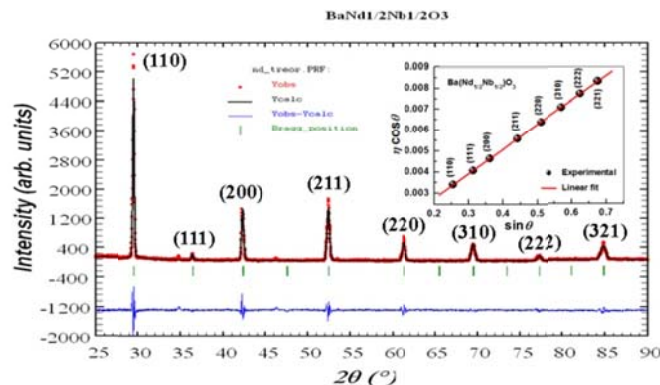


Fig. 6 Scaling behaviour of  $Z''$ . Inset: temperature dependence of relaxation time of Ba(Nd<sub>1/2</sub>Nb<sub>1/2</sub>)O<sub>3</sub> ceramic

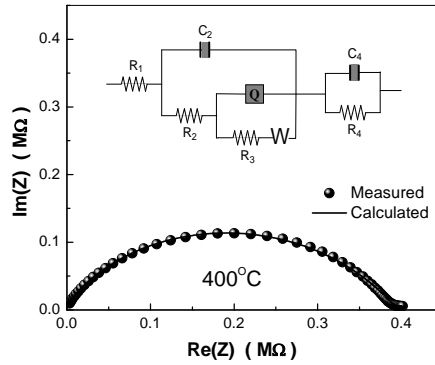


Fig. 7 Complex impedance plot of  $Ba(Nd_{1/2}Nb_{1/2})O_3$  ceramic at  $400^\circ C$ . Inset: appropriate equivalent electrical circuit

Table 2 Resulting parameters of fitting corresponding to equivalent circuit of Fig. 7

Parameters	$Ba(Nd_{1/2}Nb_{1/2})O_3$
$R_1$ ( $\Omega$ )	$1.154 \times 10^3$
$R_2$ ( $\Omega$ )	1.609
$R_3$ ( $\Omega$ )	$1.001 \times 10^{-7}$
$R_4$ ( $\Omega$ )	$7.881 \times 10^4$
$C_2$ (F)	$1.238 \times 10^{-11}$
$C_4$ (F)	$3.580 \times 10^{-10}$
CPE, $Q$ ( $S \text{ sec}^{0.5}$ )	$3.098 \times 10^{-6}$
Frequency power ( $n$ )	$6.764 \times 10^{-13}$
Warburg, $W$ ( $S \text{ sec}^{0.5}$ )	$1.325 \times 10^{-8}$

Fig. 7 depicts a complex impedance spectrum along with the appropriate equivalent circuit (inset) and its fitting at  $400^\circ C$ . It is observed that the complex plane plots of impedance data not always yield perfect or depressed semicircular arcs often the arc is asymmetric. Ideally impedance data should fit to the equivalent circuit containing two parallel combination of resistance and capacitance {of type  $R_1(C_1R_2)(C_2R_3)$ }, but they fit excellently well with the equivalent circuit of type  $R_1(C_2(R_2(Q(R_3W))))(C_4R_4)$  (inset Fig. 7) which clearly indicates the grain and grain boundary contributions. Here  $R$ ,  $C$ ,  $Q$  and  $W$  are resistance, capacitance, constant phase element and warburg element, respectively. Admittance of the CPE can be written as  $Y_{CPE} = Y_o(j\omega)^n$  where  $Y_o$  is constant pre-factor and  $n$  is exponent. Warburg admittance is defined as  $Y_w(\omega) = \sqrt{\omega} / [W(1-j)]$ , where  $j = \sqrt{-1}$  is the imaginary unit. The fitting parameters are summarized in Table 2 and were determined using a non-linear least-square fitting algorithm (Boukamp 2004). The introduction of constant phase element in the equivalent circuit may be due to the distribution of reaction rates and/or surface roughness. The Warburg impedance element may be due to the semi-infinite linear diffusion i.e., unrestricted diffusion to a large planar electrode, which obeys second Fick's law (Prasad *et al.* 2010b). Further, for Debye type relaxation, the centre of semicircular plots should be located on the  $Z'$ - axis, whereas for a non-Debye type relaxation these complex plane plots are

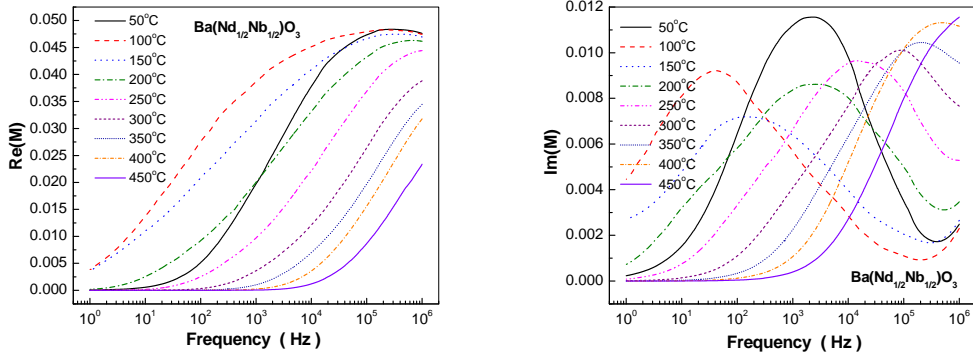


Fig. 8 Frequency dependence of real and imaginary parts of electric modulus of Ba(Nd<sub>1/2</sub>Nb<sub>1/2</sub>)O<sub>3</sub> ceramic at different temperatures

close to semicircular arcs with their centers lie below this axis. The complex impedance in such a case can be described as

$$Z^*(\omega) = Z' + iZ'' = R/[1 + (i\omega/\omega_0)^{1-\alpha}] \quad (1)$$

where  $\alpha$  represents the magnitude of the departure of the electrical response from an ideal condition and this can be determined from the location of the centre of the semicircles. Further, it is known that when  $\alpha$  approaches to zero i.e.,  $\{(1-\alpha) \rightarrow 1\}$ , Eq. (1) gives rise to classical Debye's formalism. It can be seen from the impedance plots that the data is not represented by full semicircle rather they are depressed one i.e., centre of semicircles lie little below the abscissa ( $Z'$ ) axis ( $\alpha > 0$ ), which increases with the rise in temperature suggesting the non-Debye type of behavior in BNN, similar to Ba(Y<sub>1/2</sub>Nb<sub>1/2</sub>)O<sub>3</sub> (Prasad *et al.* 2010a) and Ba(La<sub>1/2</sub>Nb<sub>1/2</sub>)O<sub>3</sub> (Prasad *et al.* 2010b). This may happen due to the presence of distributed elements in the material-electrode system.

### 3.4 Electric modulus study

Fig. 8 shows the variation of real ( $M'$ ) and imaginary ( $M''$ ) parts of electric modulus of BNN with frequency at different temperatures. It is characterized by very low value of  $M'$  in the low frequency region and a sigmoidal increase in the value of  $M'$  with the frequency approaching ultimately to  $M_\infty$ , may be attributed to the conduction phenomena due to short-range mobility of charge carriers. The variation  $M''$  as a function of frequency is characterized by: (i) clearly resolved peaks in the pattern appearing at unique frequency at different temperatures, (ii) significant asymmetry in the peak with their positions lying in the dispersion region of  $M'$  vs. frequency pattern and (iii) the peak positions have a tendency to shift towards higher frequency side with the rise in temperature. The low frequency side of the  $M''$  peak represents the range of frequencies in which charge carriers can move over a long distance i.e., charge carriers can perform successful hopping from one site to the neighbouring site. The high frequency side of the  $M''$  peak represents the range of frequencies in which the charge carriers are spatially confined to their potential wells and thus could be made localized motion within the well. The region where

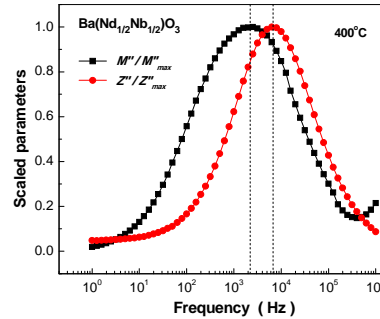


Fig. 9 Variation of normalized  $Z'$  and  $M''$  with frequency at  $400^\circ\text{C}$  for  $Ba(Nd_{1/2}Nb_{1/2})O_3$  ceramic

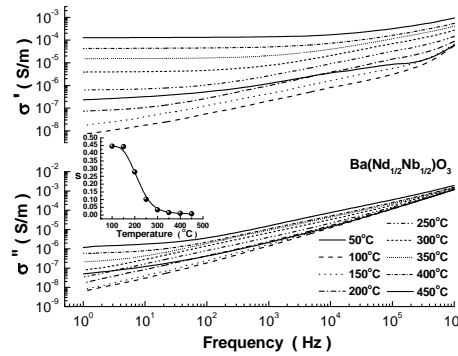


Fig. 10 Variation of real and imaginary parts of ac conductivity with frequency at different temperatures for  $Ba(Nd_{1/2}Nb_{1/2})O_3$  ceramic. Inset: variation of  $s$  with temperature

peak occurs is an indicative of the transition from long-range to short-range mobility with increase in frequency. Further, the appearance of peak in modulus spectrum provides a clear indication of conductivity relaxation. Also,  $M''(\omega)$  curves get broadened upon increasing temperature suggesting an increase in non-Debye behaviour. This particular behaviour appears to be unique to electrical relaxation since all other relaxation processes (e.g., mechanical, light scattering) typically exhibit opposite behaviour with tendency towards Debye behaviour with increasing temperature (Prasad *et al.* 2007).

Fig. 9 shows the variation of scaled parameters ( $Z''/Z''_{\max}$  and  $M''/M''_{\max}$ ) with frequency at  $400^\circ\text{C}$ . It is observed that the peaks are not occurring at the same frequency, indicating an evidence of change in apparent polarization. The overlapping of peaks is an evidence of long-range conductivity whereas the difference is an indicative of short-range conductivity, *via* hopping type of mechanism (Cao and Gerhardt 1990, Gerhardt 1994, Nobre and Lanfredi 2003).

### 3.5 Ac conductivity studies

Fig. 10 shows the log–log plots of real ( $\sigma'$ ) and imaginary ( $\sigma''$ ) parts of ac electrical conductivity versus frequency at different temperatures. The  $\sigma'-f$  plots show dispersion throughout

the chosen frequency range and with the increment in temperature plots get flattened (plateau value). The switch from the frequency independent to the dependent regions shows the onset of the conductivity relaxation phenomenon which indicates the translation from long range hopping to the short range ion motion. Furthermore, the real part of electrical conductivity, in most of the materials due to localized states is expressed as a power law:  $\sigma'(\omega) = \sigma_0 + A\omega^s$ , where  $\sigma_0$  is the frequency independent (electronic or dc) part of ac conductivity,  $0 \leq s \leq 1$  is the index,  $\omega (=2\pi f)$  is angular frequency of applied ac field and  $A [= \pi N^2 e^2 / 6k_B T (2a)]$  is a constant,  $e$  is the electronic charge,  $T$  is the temperature,  $a$  is the polarisability of a pair of sites, and  $N$  is the number of sites per unit volume among which hopping takes place. Such variation is associated with displacement of carriers which move within the sample by discrete hops of length  $R$  between randomly distributed localised sites. The term  $A\omega^s$  can often be explained on the basis of two distinct mechanisms for carrier conduction: quantum mechanical tunneling (QMT) through the barrier separating the localised sites and correlated barrier hopping (CBH) over the same barrier. In these models, the exponent  $s$  is found to have two different trends with temperature and frequency. If the ac conductivity is originated from QMT,  $s$  is predicted to be temperature independent but expected to show a decreasing trend with  $\omega$ , while for CBH, temperature dependence of  $s$  should show a decreasing trend. The values of the index  $s$  were obtained from the slopes of the plots in the low frequency region. The inset of Fig. 10 shows the temperature dependence of  $s$ . It can be seen that the value of  $s$  is always less than 1 and decreases with the rise in temperature. Also, the value of  $s$  approaching to zero at higher temperatures indicates that the dc conductivity dominates at higher temperatures in the low frequency region following power law. The model based on correlated hopping of electrons over barrier, predicts a decrease in the value of the index with the increase in temperature and so this is consistent with the experimental results. Therefore, the conduction in the system may be considered to be due to the short range translational type hopping of charge carriers. This indicates that the conduction process is a thermally activated process. The imaginary part of the ac conductivity decreases with decreasing frequency and at higher temperature it finds almost plateau value in lower frequency side which supports the electronic conduction in BNN.

Hopping conduction mechanism is generally consistent with the existence of a high density of states in the materials having band gap like that of semiconductor. Owing to localisation of charge carriers, formation of polarons takes place and the hopping conduction may occur between the nearest neighboring sites. Fig. 11 shows the variation of ac conductivity versus  $10^3/T$ . The apparent activation energy for conduction was obtained using the Arrhenius relationship

$$\sigma'(\omega) = \sigma_0 \exp(-E_a / k_B T) \quad (2)$$

A linear least square fitting of the conductivity data to Eq. (2) gives the value of the apparent activation energy  $E_a$ . The values of  $E_a$  at higher temperatures are found to be 0.25, 0.17 and 0.074 eV at 1 Hz, 1 kHz and 1 MHz, respectively. The low value of  $E_a$  may be due to the carrier transport through hopping between localised states in a disordered manner (Prasad *et al.* 2010c). The enhancement in conductivity with temperature may be considered on the basis that within the bulk, the oxygen vacancies due to the loss of oxygen are usually created during sintering and the charge compensation follows the equation (Kroger and Vink 1956):  $O_o \rightarrow \frac{1}{2}O_2 \uparrow + V_o^{\bullet\bullet} + 2e^-$ , which may leave behind free electrons making them n-type.

Ac conductivity data have been used to evaluate the density of states at Fermi level  $N(E_f)$  based on correlated barrier hopping model using the relation (Sharma *et al.* 2003):

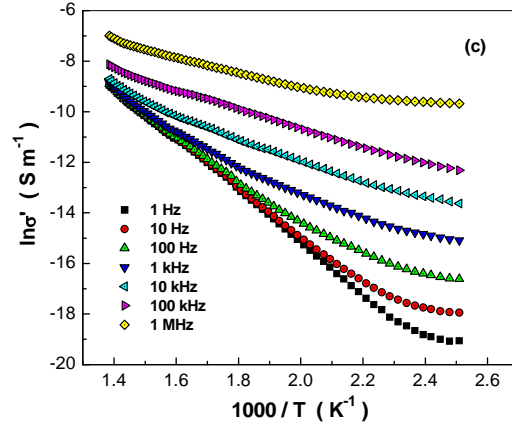


Fig. 11 Variation of real part of ac conductivity with temperature at different frequencies for  $Ba(Nd_{1/2}Nb_{1/2})O_3$  ceramic

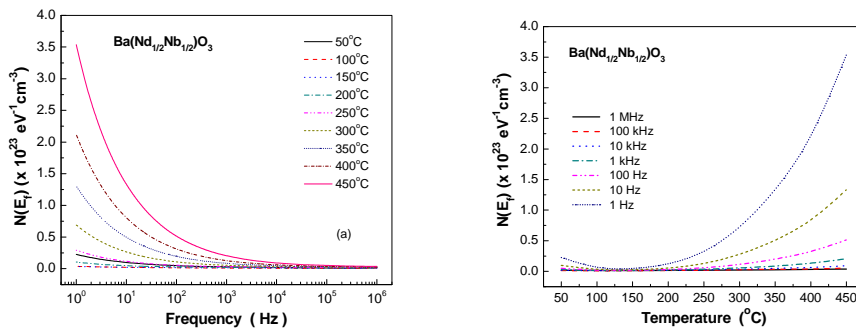


Fig. 12(a) Frequency dependence of  $N(E_f)$  at different temperatures and (b) Temperature dependence of  $N(E_f)$  at different frequencies of  $Ba(Nd_{1/2}Nb_{1/2})O_3$  ceramic

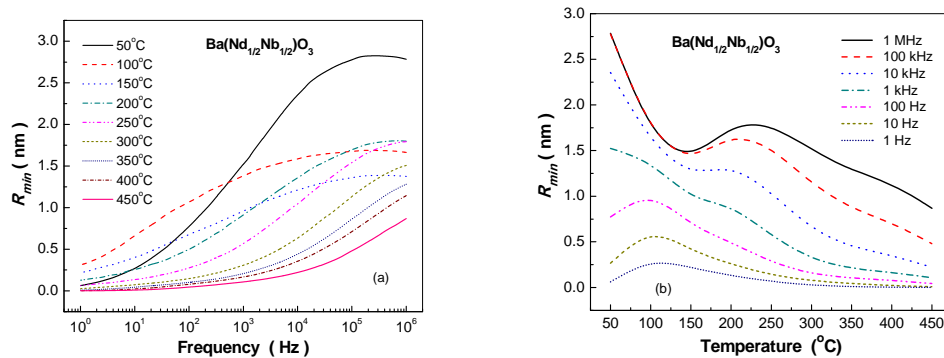


Fig. 13(a) Frequency dependence of  $R_{min}$  at different temperatures and (b) Temperature dependence of  $R_{min}$  at different frequencies of  $Ba(Nd_{1/2}Nb_{1/2})O_3$  ceramic

$\sigma' = (\pi/3)e^2\omega k_B T [N(E_f)]^2 \alpha^{-5} [\ln(f_o/\omega)]^4$ , where  $f_o$  the photon frequency and  $\alpha$  is the localized wave function, assuming  $f_o = 10^{13}$  Hz, the polarisability  $\alpha = 10^{10} \text{ m}^{-1}$  at various operating frequencies and temperatures. Fig. 12(a) illustrates the frequency dependence of  $N(E_f)$  at different temperatures. It can be seen that the values of  $N(E_f)$  decrease with increasing operating frequency for all temperatures and almost merge above 40 kHz. Fig. 12(b) shows the variation of  $N(E_f)$  with temperature at different frequencies. It is seen that the values of  $N(E_f)$  simply increases with the increase in temperature. Therefore, at low frequencies the electrical conduction in the system is affected by both frequency as well as temperature, whereas at higher frequencies the charge carriers are localised and being affected by thermal excitations. The reasonably high values of  $N(E_f)$  suggest that the hopping between the pairs of sites dominates the mechanism of charge transport in BNN (Bhagat and Prasad 2010, Prasad *et al.* 2010d). The minimum hopping length,  $R_{min}$  was estimated using the relation (Nadeem *et al.* 2002):  $R_{min} = 2e^2/\pi\epsilon\epsilon_0 W_m$ , where  $W_m \{= 6k_B T/(1-s)\}$  is the binding energy. Fig. 13(a) shows the variation of  $R_{min}$  with frequency at different temperatures. It is characterised by very low value ( $\sim 10^{-10}$  m) of  $R_{min}$  in the low frequency region, a continuous dispersion with increasing frequency having a tendency to saturate at a maximum asymptotic value in the high frequency region. Such observations may possibly be related to a lack of restoring force governing the mobility of charge carriers under the action of an induced electric field. This behaviour supports long range mobility of charge carriers. Further, a sigmoidal increase in the value of  $R_{min}$  with the frequency approaching ultimately to a saturation value, may be attributed to the conduction phenomenon due to short-range mobility of charge carriers (Prasad *et al.* 2010b, Prasad *et al.* 2010d). Fig. 13(b) presents the variation of  $R_{min}$  with temperature at different frequencies. It can be seen that the values of  $R_{min}$  decrease with temperature at lower frequencies and it finds a maximum which supports above observations. Also, the value of  $R_{min}$  was found to be  $\sim 10^{-3}$  times smaller in comparison to the grain size of BNN.

#### 4. Conclusions

Polycrystalline  $\text{Ba}(\text{Nd}_{1/2}\text{Nb}_{1/2})\text{O}_3$  prepared using high temperature solid state reaction method, was found to possess a perovskite type cubic structure with the space group  $Pm\bar{3}m$ . The dielectric relaxation was found to be of non-Debye type. The ac conductivity is found to obey the universal power law and showed the NTCR character. The correlated barrier hopping model is found to successfully explain the mechanism of charge transport in  $\text{Ba}(\text{Nd}_{1/2}\text{Nb}_{1/2})\text{O}_3$ . The results are well supported by density of states at Fermi level and scaled parameters data. The minimum hopping length was found to be  $\sim 10^{-3}$  times smaller in comparison to the grain size.

#### Acknowledgements

The present work was supported by Defense Research and Development Organization, New Delhi.

#### References

AmarNath, K., Prasad, K., Chandra, K.P. and Kulkarni, A.R. (2012), "Impedance and ac conductivity studies

- of  $Ba(Pr_{1/2}Nb_{1/2})O_3$  ceramic”, *Bull. Mater. Sci.* (in print)
- Bhagat, S. and Prasad, K. (2010), “Structural and impedance spectroscopy analysis of  $Ba(Fe_{1/2}Nb_{1/2})O_3$  ceramic”, *Phys. Status Solidi (a)*, **207**, 1232-1239.
- Boukamp, B.A. (2004), “Electrochemical impedance spectroscopy in solid state ionics: recent advances”, *Solid State Ionics*, **169**, 65-73.
- Cao, W. and Gerhardt, R. (1990), “Calculation of various relaxation times and conductivity for a single dielectric relaxation process”, *Solids State Ionics*, **42**, 213-221.
- Dias, A., Abdul Khalam, L., Sebastian, M.T., Paschoal, C.W.A. and Moreira, R.L. (2006), “Chemical substitution in  $Ba(RE_{1/2}Nb_{1/2})O_3$  (RE = La, Nd, Sm, Gd, Tb, and Y) microwave ceramics and its influence on the crystal structure and phonon modes”, *Chem. Mater.*, **18**, 214-220.
- Gerhardt, R. (1954), “Impedance and dielectric spectroscopy revisited: distinguishing localized relaxation from long-range conductivity”, *J. Phys. Chem. Solids*, **55**, 1491-1506.
- Khalam, L.A., Sreemoolanathan, H., Ratheesh, R., Mohanan, P. and Sebastian, M.T. (2004), “Preparation, characterization and microwave dielectric properties of [B' = La, Pr, Nd, Sm, Eu, Gd, Tb, Dy, Ho, Y, Yb and In] ceramics”, *Mater. Sci. Eng. B*, **107**, 264-270.
- Khalam, L.A. and Sebastian, M.T. (2006), “Microwave dielectric properties of [B' = La, Pr, Nd, Sm, Eu, Gd, Tb, Dy, Ho, Y, Er, Yb, and In] ceramics”, *Int. J. Appl. Ceram. Technol.*, **3**, 364-374.
- Kröger, F.A. and Vink, H.J. (1956), “Relations between the concentrations of imperfections in crystalline solids”, *Solid State Phys.*, **3**, 307-435.
- Nadeem, M., Akhtar, M.J., Khan, A.Y., Shaheen, R. and Haque, M.N. (2002), “Ac study of 10% Fe-doped  $La_{0.65}Ca_{0.35}MnO_3$  material by impedance spectroscopy”, *Chem. Phys. Lett.*, **366**, 433-439.
- Nobre, M.A.L. and Lanfredi, S. (2003), “Dielectric spectroscopy on  $Bi_3Zn_2Sb_3O_{14}$  ceramic: an approach based on the complex impedance”, *J. Phys. Chem. Solids*, **64**, 2457-2464.
- Prasad, K., Kumar, A., Choudhary, S.N. and Choudhary, R.N.P. (2005), “Relaxor behaviour of  $Pb[(Mg_{3/4}Co_{1/4})_{1/3}Nb_{2/3}]O_3$  ceramic”, *Solid State Ionics*, **176**, 1641-1646.
- Prasad, K., Kumari, K., Lily, Chandra, K.P., Yadav, K.L. and Sen, S. (2007), “Electrical conduction in  $(Na_{0.5}Bi_{0.5})TiO_3$  ceramic: Impedance spectroscopy analysis”, *Adv. Appl. Ceram.*, **106**, 241-246.
- Prasad, K., Bhagat, S., Priyanka, AmarNath, K., Chandra, K.P. and Kulkarni, A.R. (2010a), “Electrical properties of  $BaY_{0.5}Nb_{0.5}O_3$  ceramic: Impedance spectroscopy analysis”, *Physica B: Condens. Matter*, **405**, 3564-3571.
- Prasad, K., AmarNath, K., Bhagat, S., Priyanka, Chandra, K.P. and Kulkarni, A.R. (2010b), “Structural and electrical properties of lead-free ceramic:  $Ba(La_{1/2}Nb_{1/2})O_3$ ”, *Adv. Appl. Ceram.*, **109**, 225-233.
- Prasad, K., Bhagat, S., AmarNath, K., Choudhary, S.N. and Yadav, K.L. (2010c), “Electrical conduction in  $Ba(Bi_{0.5}Nb_{0.5})O_3$  ceramic: impedance spectroscopy analysis”, *Mater. Sci.-Poland*, **28**, 317-325.
- Prasad, K., Chandra, K.P., Bhagat, S., Choudhary, S.N. and Kulkarni, A.R. (2010d), “Structural and electrical properties of lead-free perovskite  $Ba(Al_{1/2}Nb_{1/2})O_3$ ”, *J. Am. Ceram. Soc.*, **93**, 190-196.
- Sharma, G.D., Roy, M. and Roy, M.S. (2003), “Charge conduction mechanism and photovoltaic properties of 1,2-diazoamino diphenyl ethane (DDE) based schottky device”, *Mater. Sci. Eng. B*, **104**, 15-25.
- Sreemoolanathan, H., Ratheesh, R., Sebastian, M.T. and Mohanan, P. (1997), “ $Ba(Tb_{1/2}Nb_{1/2})O_3$ : a new ceramic microwave dielectric resonator,” *Mater. Lett.*, **33**, 161-165.
- Zurmiühlen, R., Petzelt, J., Kamba, S., Voitsekhovskii, V.V., Colla, E. and Setter, N. (1995a), “Dielectric spectroscopy of , complex perovskite ceramics: Correlations between ionic parameters and microwave dielectric properties. I. Infrared reflectivity study (10<sup>12</sup>-10<sup>14</sup> Hz),” *J. Appl. Phys.*, **77**, 5341-5350.
- Zurmiühlen, R., Petzelt, J., Kamba, S., Kozlov, G., Volkov, A., Gorshunov, B., Dube, D., Tagantsev, A. and Setter, N. (1995b), “Dielectric spectroscopy of  $Ba(B'_{1/2} B''_{1/2})O_3$ , complex perovskite ceramics: correlations between ionic parameters and microwave dielectric properties. II. Studies below the phonon eigenfrequencies (10<sup>2</sup>-10<sup>12</sup> Hz),” *J. Appl. Phys.*, **77**, 5351-5364.